Electronic Supplementary Material (ESI) for Journal of Materials Chemistry A.

Supplementary Information

Yolk-Shell Co_2CrO_4 Nanospheres as Highly Catalysts for Li-O_2 Batteries: Understanding of Electrocatalytic Mechanism

Qin Zhao,[a] Caixia Wu,[b] Lina Cong,[a] Yuhang Zhang,[a] Guiru Sun,[a] Haiming Xie,[ab] Liqun Sun*[a] and Jia Liu[a]*

[a]National & Local United Engineering Laboratory for Power Batteries and [b]Key Laboratory of Polyoxometalate Science of Ministry of Education, Faculty of Chemistry, Northeast Normal University, Changchun 130024, P. R. China

*To whom correspondence should be addressed to H. X. (Email: xiehm136@nenu.edu.cn) or L. S. (Email: sunlq446@nenu.edu.cn)

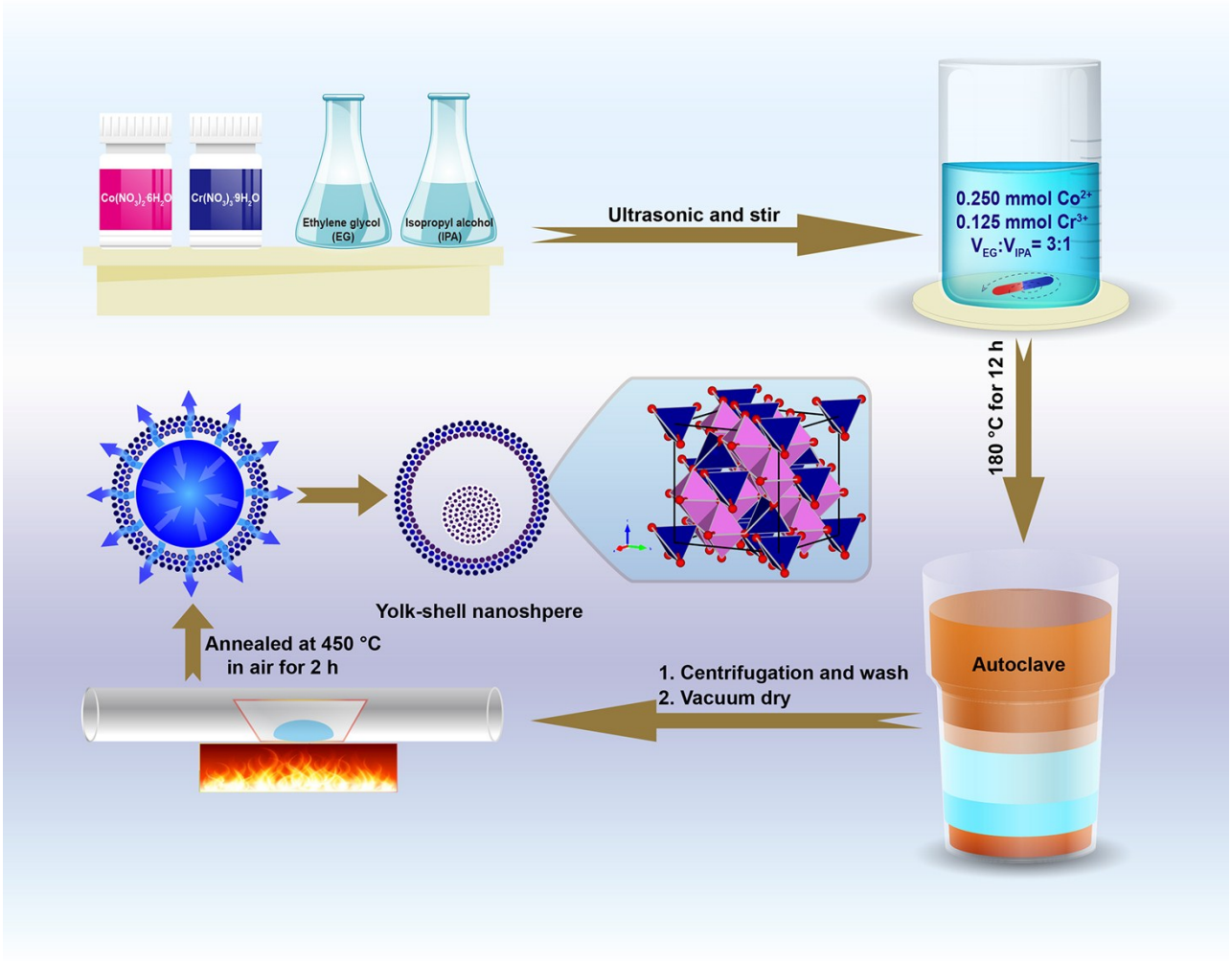

Scheme S1. Schematic illustration of the preparation process of yolk-shell CCO nanospheres.

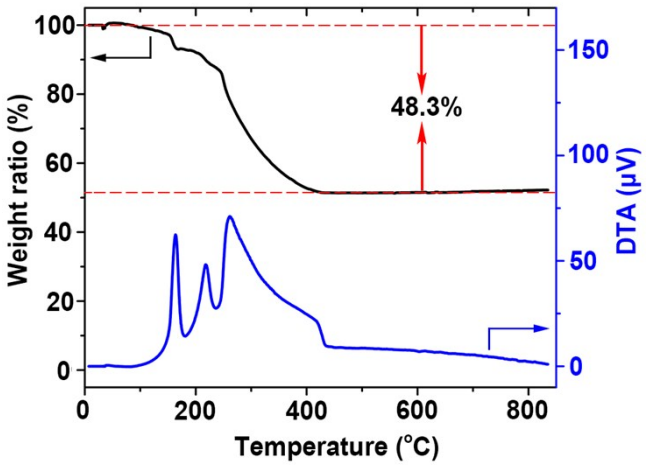

Fig. S1. Thermogravimetry (TG) and differential thermal analysis (DTA) curves of Co-Cr precursor at a heating rate of 10 °C min^{-1} under air atmosphere over the temperature range 30 - 800 °C.

Fig. S1 presents the TG-DTA curves of Co-Cr precursor in air. Weight loss from 30 to 170 °C corresponds to H_2O evaporation. From 170 to 245 °C with an endothermic DTA peak at 218 °C corresponds to a partial dehydration.[1] Weight loss from 245 to 425 °C with two endothermic DTA peaks at 261 and 422 °C correspond to the oxidative decomposition of the metallic complexes and crystallization of amorphous Co-Cr Oxide, respectively.[2] After 425 °C, the curve has no weight loss process, indicating that the Co-Cr precursor was completely converted to CCO and the total weight loss was 48.3 %. Hence, we choose 450 °C as the calcination temperature to ensure CCO formation.

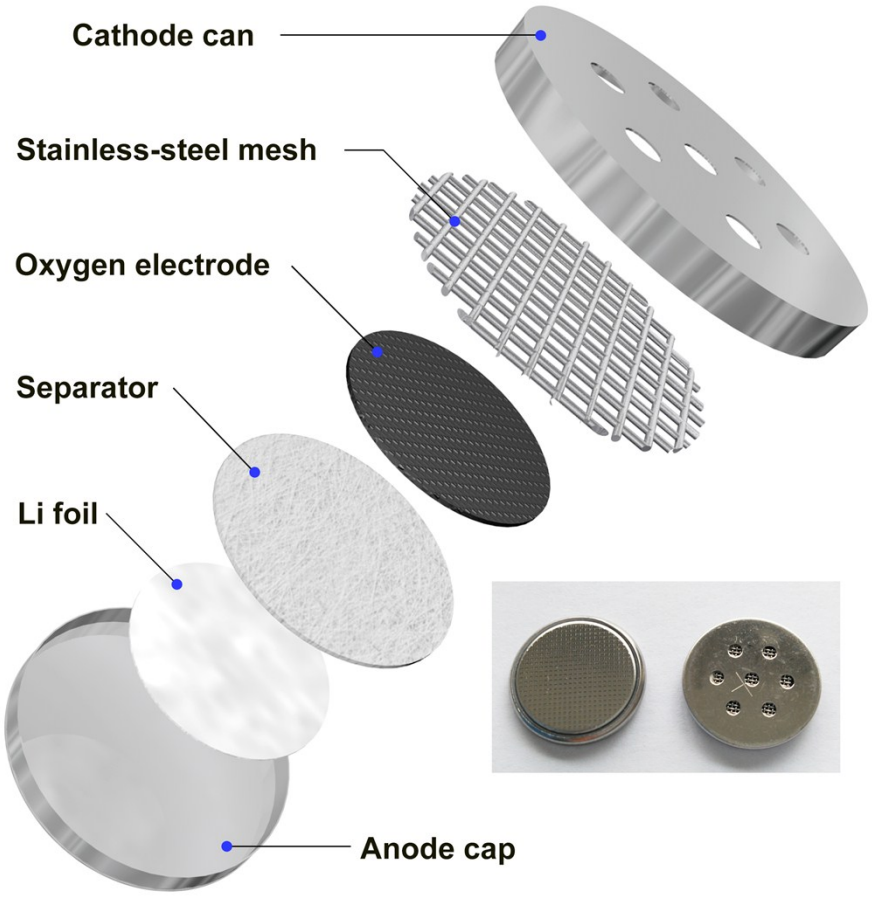

Scheme S2. Schematic illustration of a Li-O_2 cell.

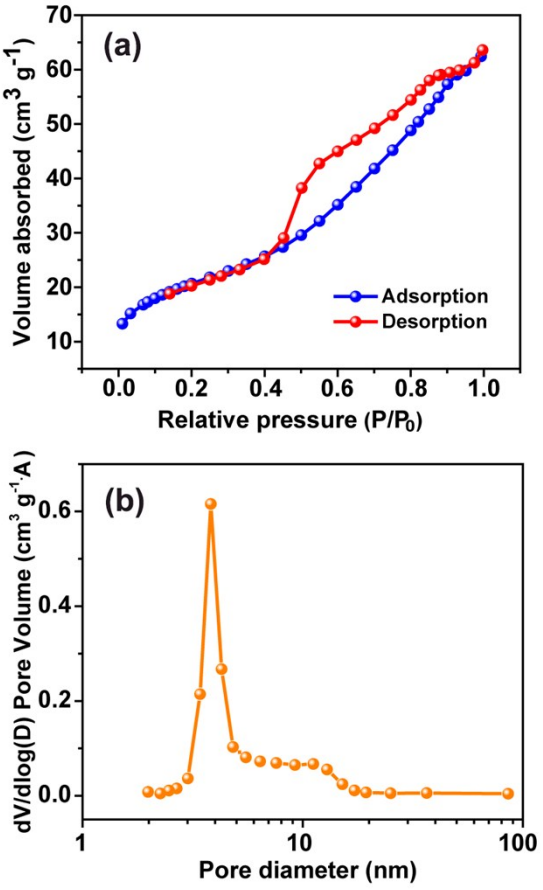

Fig. S2. (a) N_2 adsorption-desorption isothermand and (b) pore size distribution of porous CCO yolk-shell nanospheres.

As can be seen in Fig. S2a, the Brunauer-Emmett-Teller (BET) specific surface area of CCO yolk-shell nanospheres is 73.8 m^2 g^{-1} and a typical mesoporous structure with type IV isotherm with H2 hysteresis loop can be deduced. The Barret-Joyner-Halenda (BJH) pore size distribution also implies the presence of mesopores (Fig. S2b). The yolk-shell mesoporous structure of CCO is benefit to O_2 diffusion and electrolyte immersion, facilitating ORR and OER in Li-O_2 batteries.

Table S1. Discharge-charge specific capacities, and coulombic efficiencies of Li-O_2 cells with CCO as catalyst and without catalyst cycled at different current densities of 100, 200, 300, and 500 mA g_{total}^{-1} within a potential range of 2.2-4.4 V *vs.* Li/Li^+.

Current Density (mA g_{total}^{-1})	Electrodes with CCO as catalyst			Electrodes without catalyst		
	Discharge (mAh g_{total}^{-1})	Charge (mAh g_{total}^{-1})	Coulombic efficiency (%)	Discharge (mAh g_{total}^{-1})	Charge (mAh g_{total}^{-1})	Coulombic efficiency (%)
100	8554	8528	99.7	4252	3560	83.7
200	6260	6220	99.3	2842	2213	77.9
300	3740	3685	98.5	1758	1378	78.4
500	2977	2931	98.4	1168	826	70.7

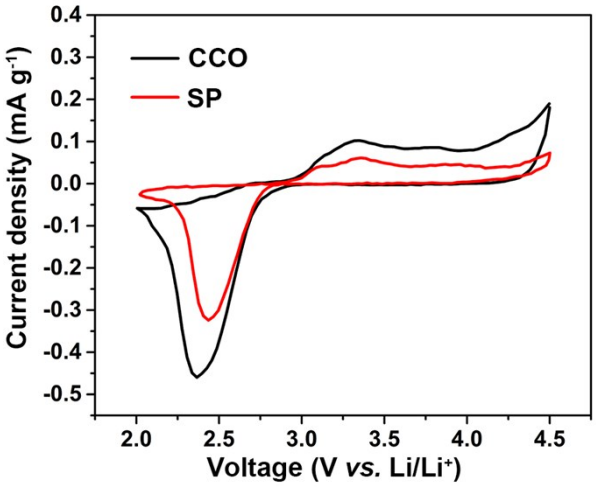

Fig. S3. Cyclic voltammetrys of Li-O_2 cells with CCO and without catalyst (SP) under O_2 atmosphere at a constant scan rate of 0.1 mV s^{-1} within a potential range of 2.0-4.5 V *vs.* Li/Li^+.

The cyclic voltammetry (CV) was used to further investigate the catalytic activities of the electrode with catalyst and without catalyst towards to ORR and OER (Fig. S3). The electrode with CCO presents a higher onset reduction potential and lower onset evolution potential as well as much larger cathodic and anodic currents than those of the electrode without catalyst, demonstrating that the employment of CCO did enhanced the reaction kinetics.

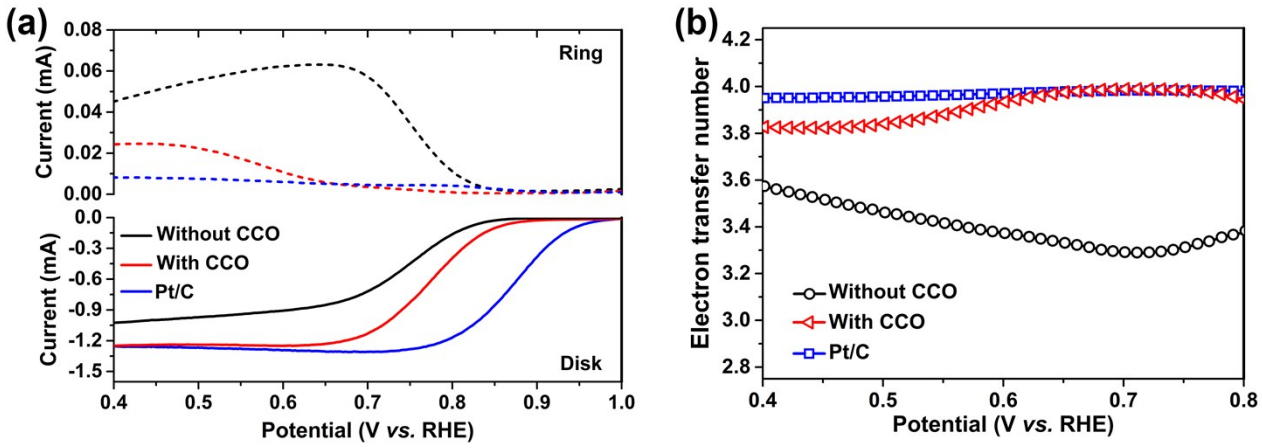

Fig. S4 (a) Rotating ring-disk electrode voltammograms recorded with CCO, without CCO and Pt/C in O_2-saturated 0.1 M KOH at 1600 rpm with a scan rate of 5 mV s^{-1}. The ring potential was constant at 1.5 V *vs*. RHE. (b) The corresponding electron transfer number of the electrodes with CCO, without CCO and Pt/C at various potentials.

To further study the ORR electrocatalytic activity of as-prepared CCO in aqueous system, rotating ring-disk electrode (RRDE) measurements were performed to monitor the formation of peroxide species (HO_2^-) in aqueous electrolyte (Fig. S4). Although the ORR polarization curve of a disk electrode shown in Fig. S4a confirmed that onset potential of CCO-based electrode was negative to that of the Pt-based electrode, the limiting current of CCO-based electrode was sharply elevated with the decrease of potential, which was comparable with that of Pt-based electrode. Compared to the electrode without CCO, the electrode with CCO exhibited a more positive onset potential and a higher limiting current. The corresponding ring electrode curves in Fig. S4a also proved the high catalytic activity towards to ORR with a low ring current for the CCO-based electrode. Fig. S4b shows the electron transfer numbers calculated from the RRDE curves, indicating that the ORR in the CCO-based system was inclined to undertake a four electron transfer pathway. Therefore, it can be established that as-prepared CCO can exhibit a considerable catalytic activity in aqueous electrolyte.

Table S2. Electrochemical performance of transition metal oxides nanomaterials reported in literature.

Catalysts	1st discharge/charge voltage	Current density	Specific capacity/terminal voltage	Cycle numbers/testing time	Ref.
Flower-like δ-MnO_2 on 3D graphene	2.70 V/3.95V	0.333 mA cm^{-2} = 193.2 mA g_{total}^{-1}	492 mAh g_{total}^{-1}/2.00 V	132/28.0 days	S1[3]
Porous $LaNiO_3$ nanocube	2.70 V/3.80 V	80 mA g_{total}^{-1}	500 mAh g_{total}^{-1}/2.00 V	75/39.0 days	S2[4]
G/meso-LaSrMnO	2.77 V/3.80 V	100 mA g_{total}^{-1}	500 mAh g_{total}^{-1}/2.25 V	50/16.7 days	S3[5]
3D hierarchical Co/CoO-graphene-carbonized melamine foam	2.75 V/--	100 mA g_{total}^{-1}	500 mAh g_{total}^{-1}/2.00 V	70/29.2 days	S4[6]
Porous Co-Mn-O nanocubes	2.65 V/4.10 V	0.16 mA cm^{-2} = 160 mA g_{total}^{-1}	500 mAh g_{total}^{-1}/2.00 V	100/25.0 days	S5[7]
$MnCo_2O_4$ anchored on P-doped hierarchical porous carbon	2.75 V/3.82 V	200 mA g^{-1}	1000 mAh g^{-1}/2.20 V	200/83.3 days	S6[8]
Porous spinel $NiCo_2O_4$	2.65 V/3.88 V	200 mA g_{carbon}^{-1}	1000 mAh g_{carbon}^{-1}/2.02 V	128/53.3 days	S7[9]
Yolk-shell Co_2CrO_4 microspheres	2.61 V/3.29 V	200 mA g_{total}^{-1}	1000 mAh g_{total}^{-1}/2.12 V	236/98.3 days	This work

[1] The voltage are relative to Li/Li^+ and the deviation of them is ± 0.05 V

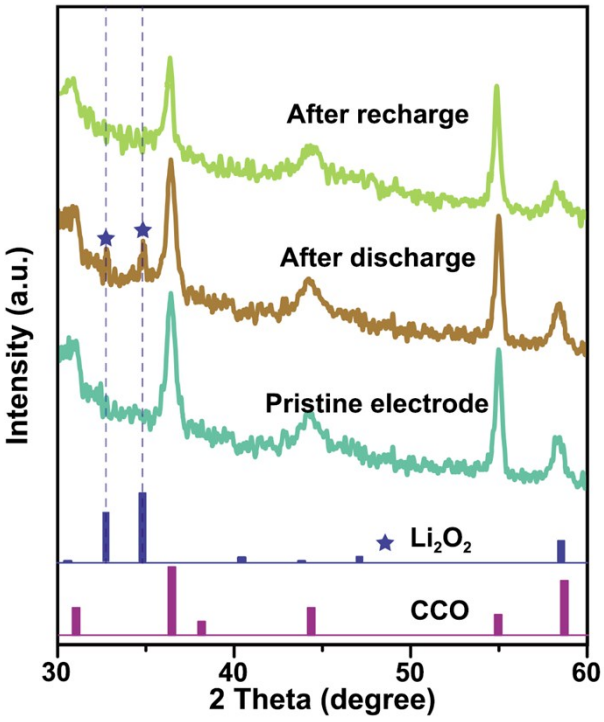

Fig. S5. XRD patterns of the pristine, discharged, and charged electrodes with CCO at a current densities of 200 mA g_{total}^{-1} within a potential range of 2.2-4.4 V *vs.* Li/Li^+.

Comparing with the pristine CCO electrode, new diffraction peaks were observed from the discharged electrode, which can be reasonably assigned as the (100) and (101) peaks of Li_2O_2 (JCPDS No. 09-0355) as highlighted in Fig. S4. The Li_2O_2 diffraction peaks disappeared after charge, demonstrating the reversible formation and decomposition of Li_2O_2 during cycling.

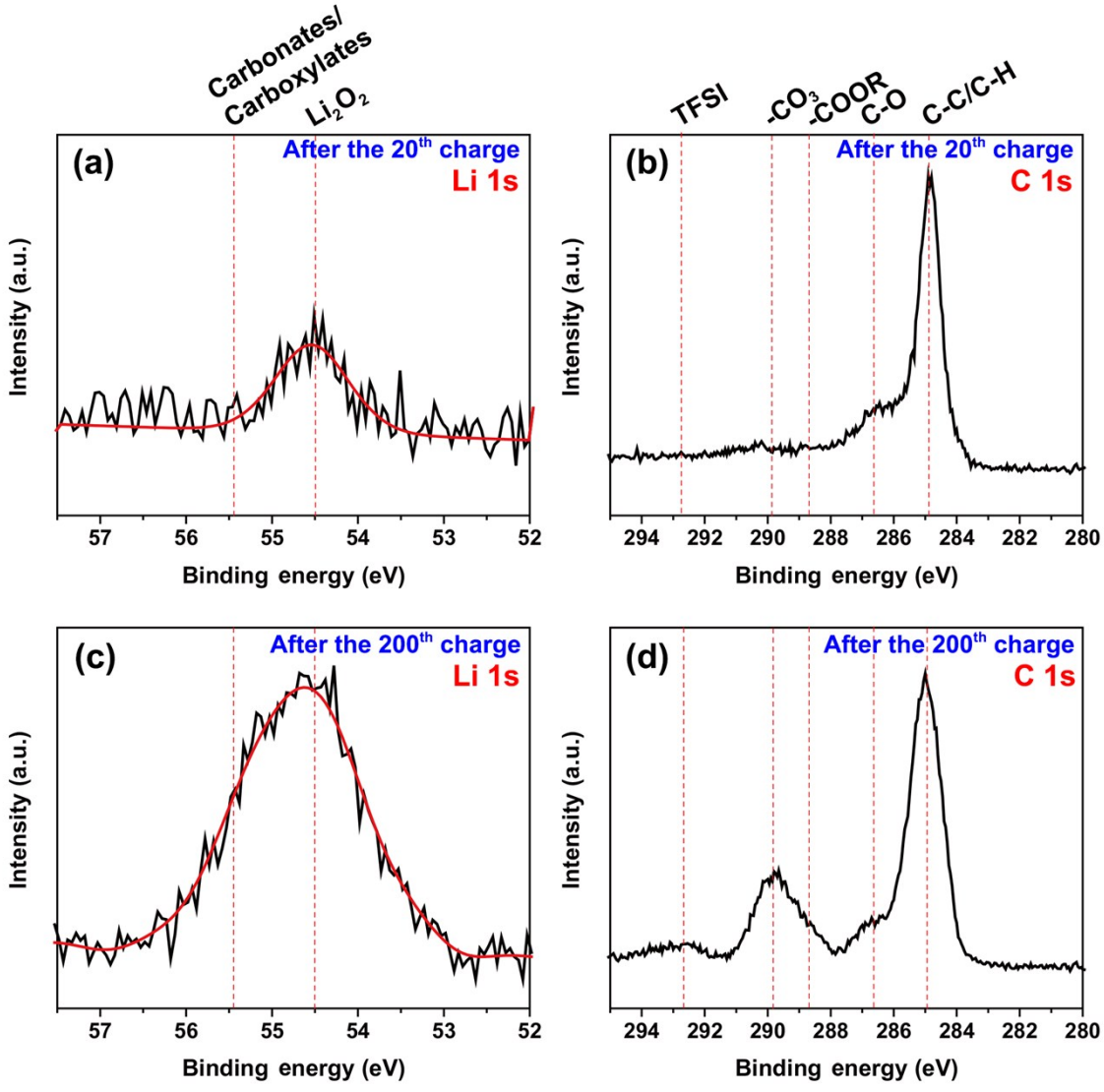

Fig. S6. XPS core level spectra of the electrodes with CCO after the 20th charge (Li 1s (a), C 1s (b)) and after the 200th charge (Li 1s (c), C 1s (d)) at a current density of 200 mA g_{total}^{-1} with a capacity limitation 1000 mAh g_{total}^{-1}.

XPS was used to identify the the composition of the residues on the electrode after charge. After the 20th charge, the primary peak of the Li 1s spectrum (54.5 eV) matches well with the location expected for Li_2O_2 (Fig. S6a).[10-12] No carbonate or carboxylate species was detected in the C 1s spectrum (Fig. S6b). This confirms that the undecomposed product is Li_2O_2 after the 20th charge. After the 200th

charge, the primary peak of the Li 1s spectrum (54.5 eV) indicated the existance of Li_2O_2, and the Li 1s peak was slightly shifted toward to 55.4 eV, which can be can be assigned to lithium carbonates and lithium carboxylates (Fig. S6c). The C 1s spectrum (Fig. S6d) further confirms the formation of C-containing side products. It has been reported that C-containing side products cannot be evolved within the typical charging potential, which deactivates the catalyst and hinders the Li_2O_2 decomposition, resulting in the increase of cell polarization and performance degradation.

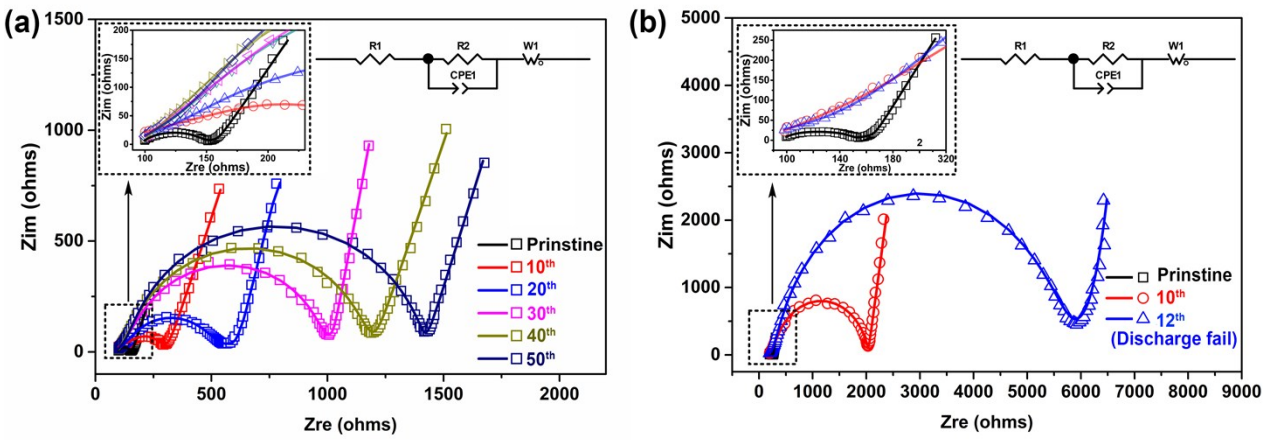

Fig. S7 Electrochemical impedance spectroscopy of the Li-O_2 cell (a) with the CCO and (b) without CCO at different cycles at a current density of 200 mA g_{total}^{-1} with a capacity limitation 1000 mAh g_{total}^{-1}.The inset figure is the corresponding equivalent circuit. The solid line was the fitting line based on the equivalent circuit.

Fig. S7 shows the Nyquist impedance plots of Li-O_2 cells with CCO and without CCO during the different cycles at a current density of 200 mA g_{total}^{-1} with a capacity limitation 1000 mAh g_{total}^{-1}.The inset is the corresponding equivalent circuit, where R1 is the ohmic resistance of the electrolyte, R2 and CPE1 represent the charge transfer resistance and the double-layer capacitance, and W1 is the Warburg impedance of Li-ion diffusion. The R2 slowly increased for the cells with CCO, which can be attributed to the residual undecomposed Li_2O_2 (Fig. S6a and b in ESI†). However, the R2 significantly increased for the cells without CCO, which might be due to the undecomposed products (carbonate and/or carboxylate species). The results demonstrate that the increase rate of the charge transfer resistance of the cell with CCO can be apparently reduced and the cycle performance can be significantly enhanced.

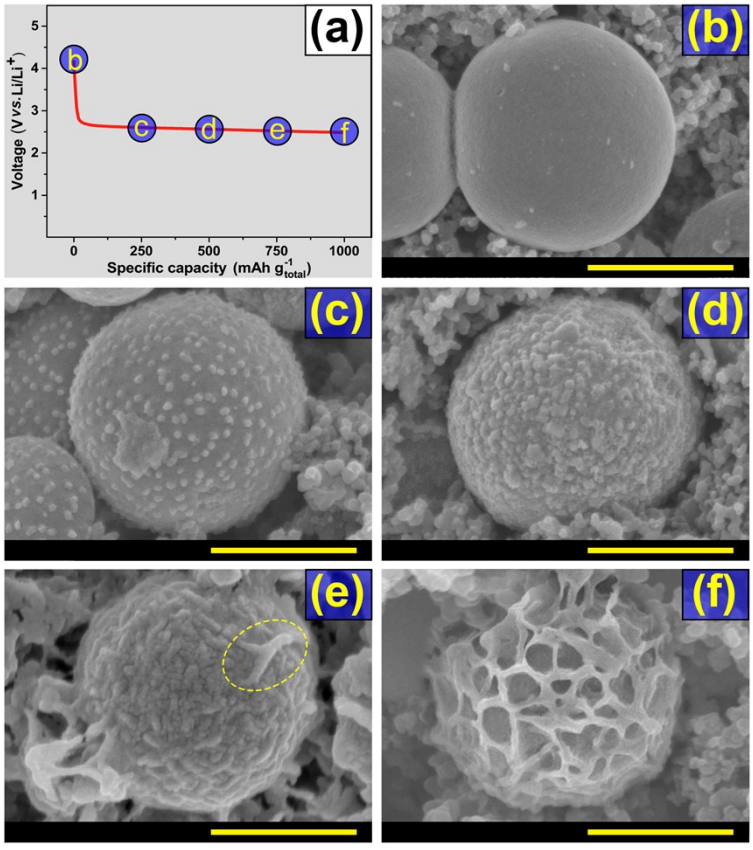

Fig. S8. (a) Discharge profile and SEM images of the electrode with CCO during the 20th discharge at a current density of 200 mA g_{total}^{-1} under the different discharge states of (b) 0 mAh g_{total}^{-1}, (c) 250 mAh g_{total}^{-1}, (d) 500 mAh g_{total}^{-1}, (e) 750 mAh g_{total}^{-1}, (f) 1000 mAh g_{total}^{-1}. (Scale bar, 500 nm)

In order to explore the formation process of Li_2O_2, SEM was applied to track the morphology evolution of Li_2O_2 during the 20th discharge process under different discharge states marked in Fig. S8a. As seen in Fig. S8b, most of Li_2O_2 was removed in the previous charge process, but a trace amount of Li_2O_2 (comfirmed by XPS (Fig. S6a and b)) can also be observed which is consistent with the observed experiment phenomena in Fig. 5g. When the delivered capacity reached 250 mAh g_{total}^{-1} (Fig. S8c), Li_2O_2 was selectivly deposited on the CCO surface, which may be attributed to the crystal plane orientation of small nanoparticles on the CCO surface. Then, the coverage of Li_2O_2 on the CCO nanosphere was expanded with the raising delivered capacity (see Fig. S8d). When the delivered capacity reached 750 mAh g_{total}^{-1}, the surface of CCO nanospheres was totally covered with Li_2O_2

and the connected Li_2O_2 can be seen in the dotted oval area marked in Fig. S8e. In the end of discharge, the flower-like Li_2O_2 was observed (Fig. S8f).

Supplementary References

1 E. Mendelovici, A. Sagarzazu and R. Villalba, *J. Therm. Anal. Calorim.*, 1993, **40**, 1115-1122.

2 M. Ştefănescu, V. Sasca and M. Birzescu, *J. Therm. Anal. Calorim.*, 1999, **56**, 579-586.

3 S. Liu, Y. Zhu, J. Xie, Y. Huo, H. Y. Yang, T. Zhu, G. Cao, X. Zhao and S. Zhang, *Adv. Energy Mater.*, 2014, **4**, 1301960.

4 J. Zhang, Y. Zhao, X. Zhao, Z. Liu and W. Chen, *Sci. Rep.*, 2014, **4**, 6005-6010.

5 Y. Yang, W. Yin, S. Wu, X. Yang, W. Xia, Y. Shen, Y. Huang, A. Cao and Q. Yuan, *ACS Nano*, 2016, **10**, 1240-1248.

6 P. Zhang, R. Wang, M. He, J. Lang, S. Xu and X. Yan, *Adv. Funct. Mater.*, 2016, **26**, 1354-1364.

7 J. Zhang, L. Wang, L. Xu, X. Ge, X. Zhao, M. Lai, Z. Liu and W. Chen, *Nanoscale*, 2015, **7**, 720-726.

8 X. Cao, J. Wu, C. Jin, J. Tian, P. Strasser and R. Yang, *ACS Catal.*, 2015, **5**, 4890-4896.

9 S. Peng, Y. Hu, L. Li, X. Han, F. Cheng, M. Srinivasan, Q. Yan, S. Ramakrishna and J. Chen, *Nano Energy*, 2015, **13**, 718-726.

10 M. A. Schroeder, A. J. Pearse, A. C. Kozen, X. Chen, K. Gregorczyk, X. Han, A. Cao, L. Hu, S. B. Lee, G. W. Rubloff and M. Noked, *Chem. Mater.*, 2015, **27**, 5305-5313.

11 Y. S. Jeong, J. B. Park, H. G. Jung, J. Kim, X. Luo, J. Lu, L. Curtiss, K. Amine, Y. K. Sun, B. Scrosati and Y. J. Lee, *Nano Lett.*, 2015, **15**, 4261-4268.

12 F. Li, D. M. Tang, Y. Chen, D. Golberg, H. Kitaura, T. Zhang, A. Yamada and H. Zhou, *Nano Lett.*, 2013, **13**, 4702-4707.